René Eisermann, Stephan Krenek*, Georg Winzer, and Steffen Rudtsch

Photonic contact thermometry using silicon ring resonators and tuneable laser-based spectroscopy

Photonische Berührungsthermometrie mit Silizium-Ringresonatoren und durchstimmbarer Laser basierter Spektroskopie

https://doi.org/10.1515/teme-2021-0054
Received March 26, 2021; accepted August 18, 2021

Abstract: Photonic sensors offer the possibility of purely optical measurement in contact thermometry. In this work, silicon-based ring resonators were used for this purpose. These can be manufactured with a high degree of reproducibility and uniformity due to the established semiconductor manufacturing process. For the precise characterisation of these photonic sensors, a measurement setup was developed which allows laser-based spectroscopy around 1550 nm and stable temperature control from 5 °C to 95 °C. This was characterised in detail and the resulting uncertainty influences of both the measuring set-up and the data processing were quantified. The determined temperature stability at 20 °C is better than 0.51 mK for the typical acquisition time of 10 s for a 100 nm spectrum. For a measurement of >24 h at 30 °C a standard deviation of 2.6 mK could be achieved. A hydrogen cyanide reference gas cell was used for traceable in-situ correction of the wavelength. The determined correction function has a typical uncertainty of 0.6 pm. The resonance peaks of the ring resonators showed a high optical quality of 157 000 in the average with a filter depth of up to 20 dB in the wavelength range from 1525 nm to 1565 nm. When comparing different methods for the determination of the central wavelength of the resonance peaks, an uncertainty of 0.3 pm could be identified. A temperature-dependent shift of the resonance peaks of approx. 72 pm/K was determined. This temperature sensitivity leads together with the analysed uncertainty contributions to a repeatability of better than 10 mK in the analysed temperature range from 10 °C to 90 °C.

Keywords: Thermometry, photonic, temperature sensor, optical ring resonator.

Zusammenfassung: Photonische Sensoren bieten die Möglichkeiten einer rein optischen Messung in der Berührungsthermometrie. In dieser Arbeit wurden hierfür siliziumbasierte Ringresonatoren verwendet. Diese lassen sich aufgrund der etablierten Halbleiterfertigung mit hoher Reproduzierbarkeit und Uniformität herstellen. Zur genauen Charakterisierung dieser photonischen Sensoren wurde ein Messplatz entwickelt, welcher eine laser-basierte Spektroskopie um 1550 nm und Thermostatisierung von 5 °C bis 95 °C ermöglicht. Dieser wurde ausführlich charakterisiert und resultierende Unsicherheitseinflüsse sowohl des Messplatzes als auch der Datenverarbeitung quantifiziert. Die ermittelte Temperatur-stabilitäten bei 20 °C ist besser als 0,51 mK für die typische Aufnahmezeit von 10 s eines 100 nm Spektrums. Für eine Messung von >24 h konnte bei 30 °C ein Standardabweichung von 2,6 mK erreicht werden. Eine Cyanwasserstoff-Referenzgaszelle diente zur rückführbaren in-situ Korrektur der Wellenlänge. Die ermittelte Korrekturfunktion hat hierbei typischerweise eine Unsicherheit von 0,6 pm. Die Resonanzpeaks der Ringresonatoren zeigten im Durschitt eine hohe optische Güte von 157 000 mit einer Filtertiefe von bis zu 20 dB im Wellenlängenbereich von 1525 nm bis 1565 nm. Beim Vergleich verschiedener Methoden zur Bestimmung der zentralen Wellenlänge der Resonanzpeaks konnte eine Unsicherheit von 0,3 pm ermittelt werden. Es wurde eine temperaturabhängige Verschiebung der Resonanzpeaks von ca. 72 pm/K bestimmt. Diese Temperatursensitivität führt mit den analysierten Unsicherheitsbeiträgen zu einer Wiederholbarkeit von besser als 10 mK im untersuchten Temperaturbereich von 10 °C bis 90 °C.

Schlagwörter: Thermometrie, Photonik, Temperatursensor, Optischer Ringresonator.

***Corresponding author: Stephan Krenek,** Physikalisch-Technische Bundesanstalt (PTB), Abbestr. 2–12, 10587 Berlin, Germany, e-mail: stephan.krenek@ptb.de, ORCID: https://orcid.org/0000-0001-9289-044X
René Eisermann, Steffen Rudtsch, Physikalisch-Technische Bundesanstalt (PTB), Abbestr. 2–12, 10587 Berlin, Germany, ORCID: https://orcid.org/0000-0001-6469-9293 (R. Eisermann)
Georg Winzer, Leibniz-Institut für innovative Mikroelektronik (IHP), Im Technologiepark 25, 15236 Frankfurt (Oder), Germany

1 Introduction

Conventional temperature measurements in the industrially relevant temperature range from about –200 °C to 850 °C (according to IEC-60751) are usually based on measuring the electrical resistance (e. g. Pt100) [1]. Especially in applications including high electromagnetic fields or in harsh environments photonic sensors offer new possibilities for temperature measurement. In contrast to electrical sensors, photonic sensors use light-matter interaction to measure temperature. For example, a temperature change leads to a change in the material-dependent refractive index. In an optical resonator, this cause a change of the resonance wavelength, which can be measured [2, 3, 4]. Two main methods are used, fibre-optic sensors (e. g. fibre Bragg gratings, FBGs) and integrated photonic sensors. In the field of fibre-optic sensing, devices for temperature sensing using FBGs are already commercially available. They are suitable to determine temperature with an uncertainty in the range of a few 100 mK [5, 6]. These sensors are mainly limited by their temperature dependent shift of about 10 pm/K together with the uncertainty in peak centre detection due to the typical *FWHM* (full width half maximum) of about 100 pm. Another solution are distributed fibre optic techniques based on backscattering processes (e. g., Rayleigh scattering) which are suitable to measure distributed temperature changes over large distances [7]. Photonic integrated circuits based on silicon [2, 3, 4, 8, 9] or silicon nitride waveguides [10] offer some advantages compared to fibre optical sensors. For example, higher temperature dependent resonance shifts (above 70 pm/K) and lower uncertainty in peak detection due to a ten-fold smaller peak width. National metrology institutes around the world are working on solutions to enable integrated photonic resonators for practical thermometry applications [2, 4, 8, 9, 10]. The realisation of a suitable test setup and the determination and reduction of the measurement uncertainty are highly demanding.

The Physikalisch-Technische Bundesanstalt (PTB) and the Leibniz Institute for Innovative Microelectronics (IHP) are working on microchip-based photonic sensors for temperature measurements within the framework of the EU-funded project "Photonic and Optomechanical Sensors for Nanoscaled and Quantum Thermometry" (PhotOQuant) [11]. The project is focused on basic research for high-precision measurements and the primary determination of temperature. For this purpose, chip-based sensors are designed, simulated, manufactured, characterised and calibrated. The production of the photonic integrated circuits (PICs) is carried out in the production grade clean room facilities of IHP using the "SG25H5_EPIC" technology [12]. For the characterisation of the manufactured silicon ring resonators and their temperature sensitivity, the measurement setup described in this article was developed and characterised at PTB. The main goal of this approach is to develop a cost-efficient measurement system which is suitable to determine temperature with an uncertainty below 10 mK in the range between 5 °C to 95 °C. In addition, the sensor read-out speed should be comparable or faster than conventional electrical sensors (sampling rate higher 1 Hz). In the future, it is intended to use this system, consisting of sensor and read-out setup, as a portable solution for photonic sensor based thermometry within industrial applications.

2 Experimental setup for the temperature-dependent optical characterisation of photonic micro resonators

2.1 Overview of the setup and basic idea

Figure 1 illustrates the basic idea of the photonic integrated circuit (PIC)-based temperature sensors together with an overview of the setup. The narrow-linewidth emission of a tuneable laser (swept-wavelength) is guided via glass fibres to the silicon waveguides. These fibre-coupled optical path additionally contains a variable attenuator and a polarization controller. Both elements are adjusted manually to reduce possible self-heating [15, 16] and polarisation-dependent effect are minimised

The fibre-to-chip coupling is achieved by using two microstructured planar grating couplers. The transmitted spectrum passing through the PIC is guided to variable gain photoreceivers and digitized by a 24-bit analog-to-digital converter with 675 kHz.

The light guidance of the PIC structures with sub-wavelength size results from the refractive index contrast between the silicon waveguide and the surrounding oxide [12, 13, 14]. A second circular waveguide (ring resonator) is evanescently coupled to the bus waveguide and works as an optical cavity. If the wavelength λ_m fits m-times ($m \in \mathbb{N}$) into the optical length ($n_{\mathrm{eff}}\, L$) the cavity is in resonance (1). The effective refractive index n_{eff} and the length of the resonator L are temperature dependent [13, 14]

$$\lambda_m = \frac{n_{\mathrm{eff}}\,(T,\,\lambda)\,L\,(T)}{m}. \tag{1}$$

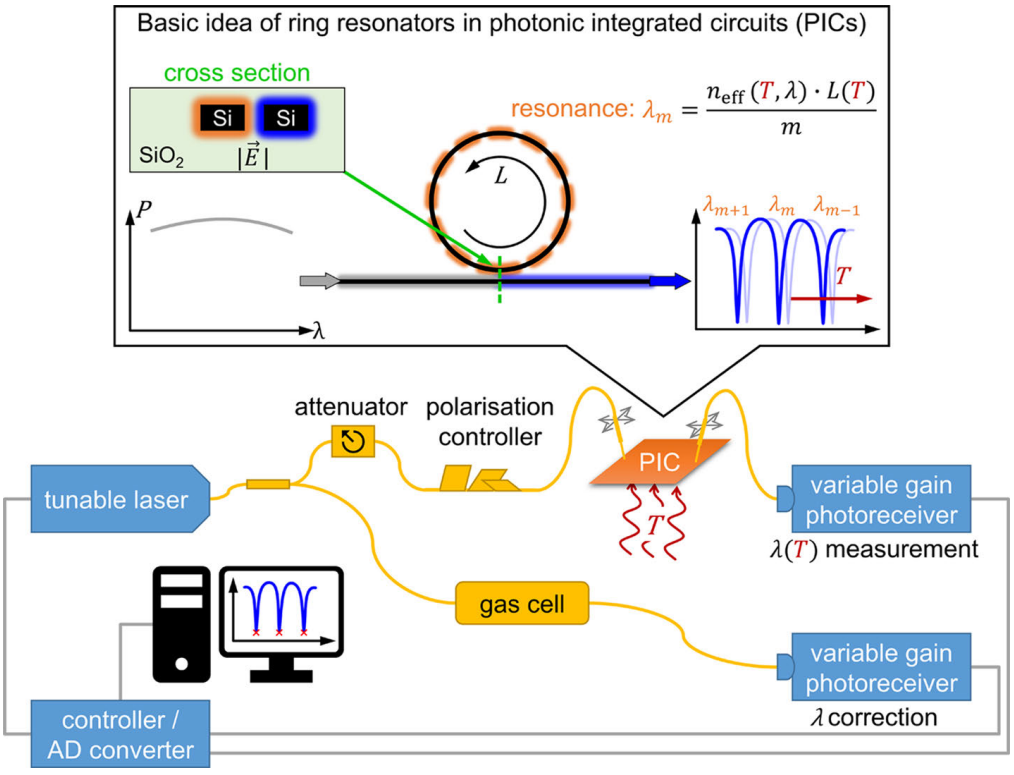

Figure 1: Schematic overview of the measurement setup for the thermal and optical characterisation of the PICs using a reference gas cell and a temperature-controlled platform. The upper part illustrates the basic idea of the PIC based thermometry to determine the temperature dependent resonance wavelength shifts of a ring resonator.

This condition leads to a multiple very narrow-band, local minima in the transmission (upper part in Fig. 1). The sharpness of the resonances is described by the quality factor Q:

$$Q_m = \frac{\lambda_m}{FWHM_m}, \tag{2}$$

with λ_m as central wavelength of the resonance m and the corresponding full width at half maximum $FWHM_m$. For temperature sensing applications a large Q-factor allows a very precise detection of the peak wavelength due to the small $FWHM$. On the other hand, a high Q-factor together with high laser power leads to increased self-heating, which limits the temperature sensitivity [15, 16]. Another important characteristic is the finesse $\mathcal{F}$ which is defined as the quotient of the free spectral range (FSR) between two resonances and the $FWHM$:

$$\mathcal{F}_m = \frac{FSR_m}{FWHM_m} = \frac{\lambda_m - \lambda_{m-1}}{FWHM_m}. \tag{3}$$

As shown in Fig. 1, the second optical path acts as wavelength reference. The laser light passes through a reference gas cell, whose absorption spectrum is used for in-situ correction of the wavelength (see Sec. 3.2). Due to the known isotopic composition and pressure, the absorption spectrum of this standard reference material (SRM) is traceable to the SI according to [17]. Finally, the data is processed as described later in this work (Secs. 3.1 and 3.2).

Alternatively, to the described swept-wavelength mode where multiple resonances m (see Eq. (1)) are measured, it is possible to lock the laser wavelength to a single resonance. To ensure a low wavelength uncertainty it is necessary to replace the gas cell for example with a wavemeter and a stabilised reference laser (see [9, 18]). However, these components significantly limit the mobility and cost-effectiveness of the setup.

For the metrological characterisation of the temperature dependent spectra two key parameter are crucial: First, a stable and traceable temperature control of the chip together with a sufficient stability of the entire measurement setup (see Fig. 1). Secondly, a high-resolution optical measurement technique with low wavelength uncertainty. In the following we describe our setup and approach for the traceable temperature and wavelength measurement.

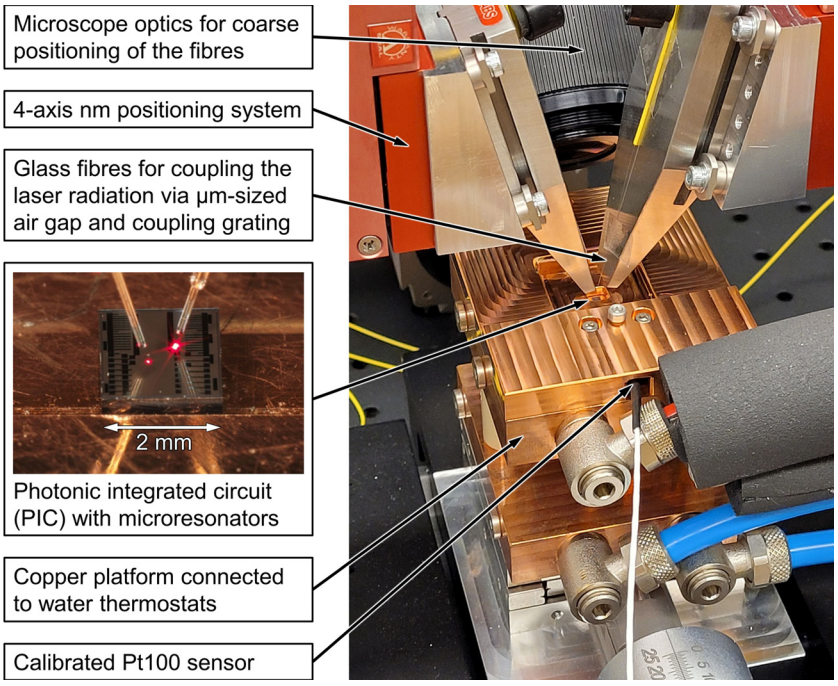

Figure 2: Experimental setup of the thermostat platform and positioning system for the characterisation of photonic resonators.

2.2 Design of the temperature-controlled platform and fibre-to-chip coupling

The setup for thermal characterization of the micro resonators was intended to meet two necessary conditions: On the one hand, the characterisation and the calibration with high temperature stability and a homogeneity in the millikelvin range at working temperatures between 5 °C and 95 °C. Normally, these requirements for temperature calibration would be realised with measurements within stirred water baths [19]. On the other hand, a stable optical coupling to integrated waveguide gratings. The necessary coupling and decoupling of the laser radiation are carried out in the current test phase with free space optical fibres. These fibres need to be adjusted a few micrometres (air gap) above the coupling grating of the chip [20]. This requires precise three-dimensional positioning of the fibres relative to the chip, with an accuracy and stability below 100 nm. Consequently, a water bath cannot be used. The precise positioning system is mounted above the temperature-controlled platform (see Fig. 2). The microscope, also shown, is used for coarse visual positioning of the fibres. The reference temperature is measured via a calibrated surface mounted Pt100 sensor clamped onto and surrounded by the thermostatted copper block (see Fig. 2). This sensor is traceable to the International Temperature Scale of 1990 (ITS-90) with an uncertainty of 8.2 mK ($k = 1$) and is measured with a resolution of 0.1 mK.

The part of the setup used for the temperature control of the photonic chip is shown in Fig. 3. The copper platforms (2) and (3) have each an independent water flow through them. For the thermal decoupling they are connected by ceramic spacers. The lower platform (3) is stabilised by a constant temperature waterflow (laboratory cold water), so that the underlying positioning unit is protected from the potentially high temperatures of the upper platform. The stable temperature of the positioning unit reduces thermal related position changes and leads to an improved position stability. The upper platform (2) is used for the active temperature control. The design is optimised for a homogeneous surface temperature. The insulated supply lines of this platform are connected to a thermostat that can precisely regulate the temperature of the water from 5 °C to 95 °C with mK stability (according to their specification). An additional copper collar (1) creates a 2 mm high side wall around the chip. These cause a more uniform temperature distribution inside the chip, as the temperature radiation losses at the sides of the chip are reduced. A vacuum tweezer (5) underneath the chip ensures secure positioning and good thermal contact with the temperature-controlled platform.

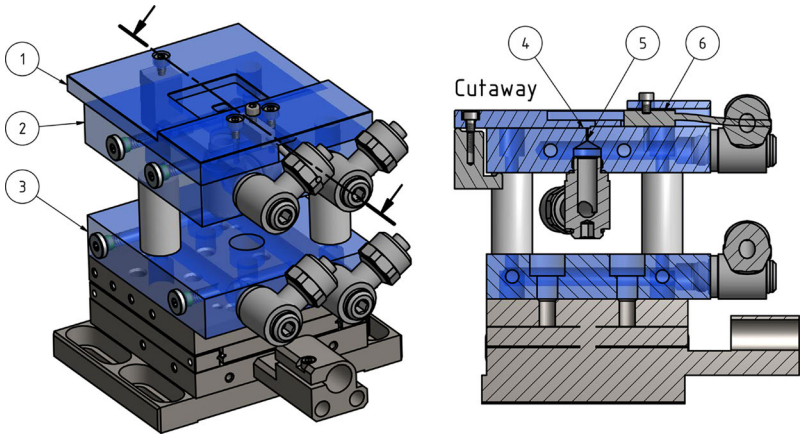

Figure 3: CAD model of the tempered platform for thermal stabilisation and characterisation of the PIC-based temperature sensors: (1) Collar, (2) Temperature controlled platform, (3) Base plate at constant temperature, (4) Position of the chip, (5) Vacuum tweezers, (6) Temperature sensor.

2.3 Characterisation and operation of the temperature-controlled platform

The stability of the thermostat platform was investigated from 10 °C to 90 °C with three different water thermostat configurations to control the temperature (see Fig. 4). The thermostats are controlled according to their internal Pt100 sensors; however, the temperature of the platform is determined with the calibrated Pt100 surface mounted sensor as described in the previous Sec. 2.2. An example of the temperature variation over 30 min and the resulting standard deviation $\pm\sigma$ (30 min) is shown in Fig. 4a for a two thermostat in series configuration (see below) at a nominal temperature of 30 °C.

For each temperature step, the standard deviation of the surface temperature over a duration of 30 min is depicted in Fig. 4b. In the first configuration the platform was connected to a heating thermostat. In this thermostat, a water bath of several litres is constantly stirred, and a part of the water is pumped through the platform. The temperature is controlled by a cooling loop and an electric heater in the water bath. Near room temperature the laboratory cold water supply (approx. 15 °C) is used for operation with higher stability. This configuration delivers a stability between 8.5 mK and 15.1 mK in the temperature range from 20 °C to 50 °C. It was found, that for temperatures above 50 °C a higher stability could be achieved without laboratory cold water supply. Therefore, the thermostat (2nd configuration) was used without additional water cooling in the temperature range from 60 °C to 90 °C. This results in a surface temperature stability of 9.1 mK to 15.3 mK over 30 min. Finally, in the third configuration we replaced the laboratory cold water supply with a cooling thermostat. This cooling thermostat can cool and heat its water bath with an integrated cooling machine between 5 °C and 95 °C. The temperature of this thermostat was set to a value that the following heating thermostat only needs about 1 % of its maximum heating power of 2.6 kW. This method with two thermostats in series shows the best stability of the surface temperature, with standard deviations between 0.7 mK and 7.4 mK for the entire temperature range from 10 °C to 90 °C (Fig. 4b). Additionally, the long-term stability was investigated for 30 °C, which results in a standard deviation of approx. 2.6 mK for a duration of 24 h. Over this period, no drift of the surface temperature was detected.

Fig. 4c shows a statistical analysis of standard deviations for 10 s segments σ_k (10 s) of the two thermostats in series configuration. These 10 s represent the acquisition time for a transmission spectrum of our PIC-based sensors, with a scan rate of 10 nm/s and a spectral bandwidth of 100 nm. The Pt100 temperature measurement speed of 1.5 s leads to 1200 of these short-term standard deviations over the total 30 min time interval. For comparison of the standard deviations investigated here for different time scales, Fig. 4a shows the band that results from the short-term standard deviations $\pm 2\sigma_k$ (10 s) around the k-th temperature value. The 10 s time interval of σ_{591} has the highest short-term standard deviation in this example and leads to the outlier in the boxplot (Fig. 4c). The mean values of the short-term standard deviations shown in the boxplots are also plotted in Fig. 4b. The values to be expected on average vary from 0.24 mK for 20 °C to 1.8 mK for 90 °C.

The whiskers of the boxplots include 95 % of the short-term standard deviations relevant for the measurement

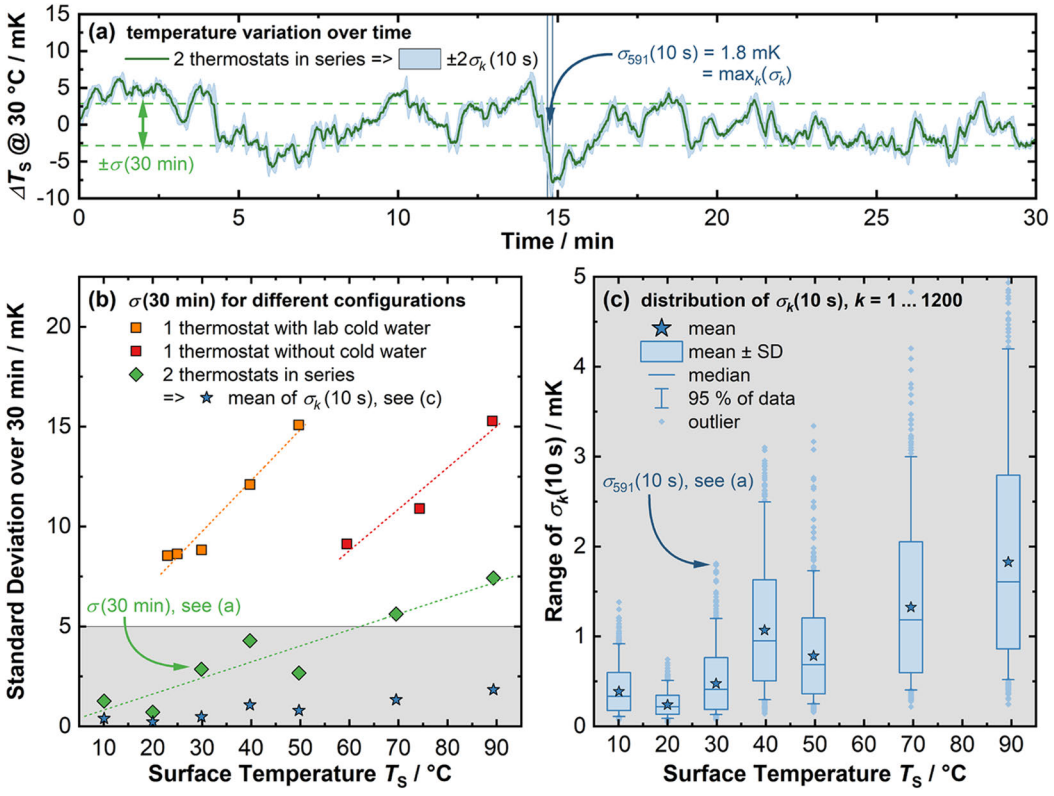

Figure 4: (a) Temperature variation of the surface temperature of the thermostat platform determined at 30 °C for 30 min for the two thermostats in series configuration. The blue band represents the $\pm 2\sigma_k$ using a sliding window of 10 s (acquisition time for a 100 nm spectrum). (b) Standard deviation of the surface temperature at different temperatures of the platform with three water bath configurations. One heating thermostat with and without lab cold water supply (approx. 15 °C), and the heating thermostat in series with a second cooling thermostat. (c) Statistical analysis of all short-term standard deviations σ_k (10 s) over the total 30 min time interval. Mean values are included in (b).

(corresponding to a $\pm 2\sigma$ interval for normal distributed data). Thus, 97.5 % of all measurements are below the upper whisker. We use these values for the estimation of the maximal uncertainty contribution of the temperature stability (see Sec. 4.2). The resulting values are between 0.51 mK for 20 °C and 4.2 mK for 90 °C. Considering a PIC temperature sensitivity of 73 pm/K this leads to a maximum temperature related wavelength shift during scan of the PIC spectrum between 0.037 pm and 0.31 pm, respectively. In summary, the thermostat platform shows sufficient stability to validate the photonic sensors.

2.4 Temperature dependent stability of the fibre to chip coupling

As described in Sec. 2.2 (see Fig. 2) a fibre coupling configuration with a small air gap is used for the characterisation of the integrated photonic circuit. To ensure an optimal power coupling between the input/output optical fibre and the photonic gratings, the positioning with submicron accuracy in all three axes, including the angle of the fibres is crucial. In our case the optimum coupling angle of 14° is provided by an angled mounted platform of the bare fibre holder, which is attached to a manual positioner with 10 nm resolution (Fig. 2). With changing temperatures of the temperature-controlled platform, the relative position between the fibre tip and the chip can change due to thermal expansion of the copper platform and the steel fibre holders. Therefore, we raised the coupling fibres between the individual temperature steps and readjusted the fibres in the temperature plateaus.

In the following we have determined relative coupling changes for different temperatures in a 100 s long time interval. The measurement condition is similar to the later shown determination of spectral transmission, except that the wavelength was kept constant at 1550 nm (outside the ring resonance).

The Fig. 5a shows the relative transmitted power for the two temperature extrema (20 °C and 90 °C). A maximum relative change below ±1 % for 20 °C (close to the 23 °C laboratory environment) and ±4 % for 90 °C was de-

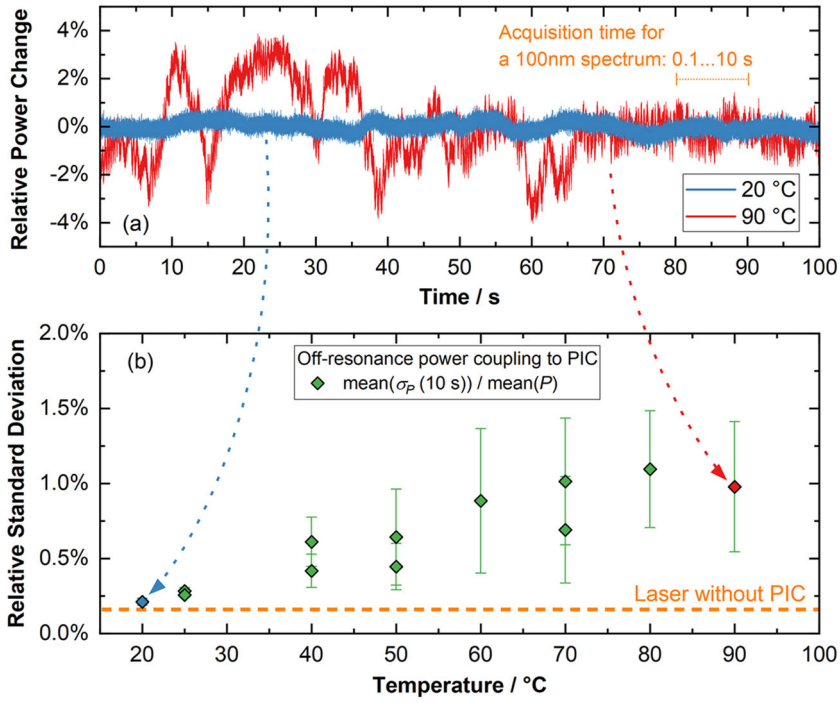

Figure 5: (a) Optical coupling stability for a nominal thermostat temperature of 20 °C and 90 °C for a 100 s long measurement. (b) Mean standard deviation of 10 s long sliding window over the 100 s measurement interval.

termined. Our typical acquisition time is between 0.1 s and 10 s for a 100 nm spectrum using a scan speeds between 10 nm/s to 1000 nm/s (Fig. 5a).

Figure 5b shows the relative standard deviation of power changes for a temperature range from 20 °C to 90 °C. The relative standard deviations were calculated from 100 short-term standard deviations using a 10 s sliding window with 9 s overlap over the full 100 s time interval. The mean of these short-term standard deviations represents the typical fluctuation within the acquisition time of 10 s. We determined a mean standard deviation of (0.21 ± 0.01) % for 20 °C and (1.0 ± 0.4) % for 90 °C.

The main causes of the observed optical power changes can be divided into three categories: mechanical, optical, and thermal relate contributions. Examples for mechanical related optical power changes are vibration and acoustic noise or air flows caused by the laboratory air conditioning. We already minimised the influence of mechanical interference in the first iteration steps of our setup. Optical related contributions are for example fluctuations of the stabilised laser power, reflections and interference or polarisation changes along the optical path. Whereas thermally induced disturbances could be thermal expansion related position changes (copper plate) or convection (at higher temperatures). The different disturbances are further discussed in Sec. 4.2 (see also Fig. 12).

One possibility to avoid coupling changes, is to glue the fibres or a fibre array directly to the chip as described in [2]. However, this has the disadvantage that a hysteresis may occur due to mechanical stress of the adhesive with changing temperatures as described by [4, 9]. Further it is reported by [9] that ageing and drift effects induced by the packaging could lead to an expanded uncertainty of 170 mK, which is the limiting factor in this work.

In summary we determine a high optical coupling stability over the full temperature range from 20 °C to 90 °C of our thermostat platform. Mean standard deviations of power coupling changes for 10 s segments of the 100 s duration are below 1.5 %. Ongoing work suggests that the coupling is suitable for even longer measurement periods (minutes to hours) without significant drift over time.

3 Data processing and evaluation

3.1 Signal processing of the photonic chip and gas cell spectra

In the following we describe the digital postprocessing of our measurement data. As can be seen in Fig. 1, we simultaneously determine the spectra of the gas cell together with the photonic chip using two variable gain photodi-

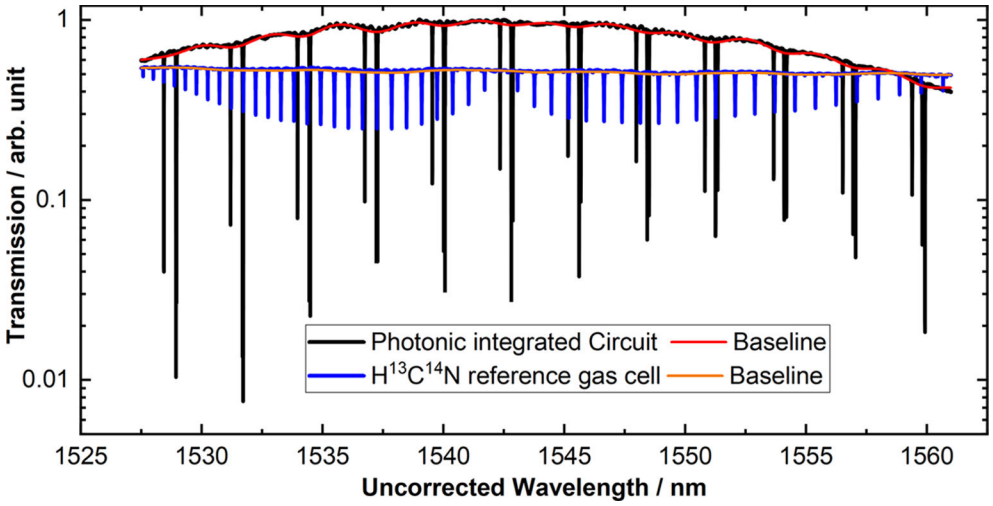

Figure 6: Raw data of the transmission spectra of the photonic integrated circuit (black) and the hydrogen cyanide ($H^{13}C^{14}N$) reference gas cell (blue). Determine baseline using a low pass filter for the PIC (red) and the gas cell (orange). The "uncorrected wavelength" refers to the internal laser wavelength detection.

odes. To ensure a time synchronisation both photodiodes use the same Analogue-digital converter (ADC) and controller. Further the laser provides a internally measured (uncalibrated) wavelength which is acquired simultaneously with the photodiodes by the controller.

Figure 6 shows the determined spectra of the gas cell and photonic chip using a scan speed of 10 nm/s and a stabilised laser power of 20 mW. To decrease nonlinear effects like self-heating the power to the photonic chip was attenuated down 10 µW using a variable optical attenuator [15, 16]. As the spectrum of the photonic chip (black line) shows, the transmission of the three micro resonators is combined with the one of grating couplers. To separate these from each other the baseline was determined using a low pass filter within the first post processing step. The baselines for both spectra are represented by the red (PIC) and orange (gas cell) curves (see in Fig. 6). Subsequently, the signal amplitude was divided by the baseline leading to relative transmission signals. Due to the high extinction ratios of the ring resonators the baseline close to the resonances is slightly to low. Since the main purpose of this baseline correction is to ensure a reasonably flat background for the later peak detection and fitting, these deviations are negligible. In the next postprocessing step the increments of the internal wavelength detection (of the laser) are corrected. As shown in Fig. 7 the wavelength values detected internally by the laser has a wavelength resolution or step size of 0.5 pm (red diamonds). This means that for a usual scan speed of 10 nm/s a minimal sampling rate of 20 kHz is required to ensure a sufficient digital sampling. The AD converter and photodiodes are suitable for a MHz sampling rate. Considering the reachable wavelength accuracy of <0.2 pm (expanded uncertainty) of the gas cell we used a digital sampling frequency (f_s) of 200 kHz, which leads to 10 amplitude values every 0.5 pm. Taking into account that in contrast to the wavelength sampling the laser is continuously tuning the wavelength, we converted the wavelength sampling to 1 amplitude value every 0.05 pm using a rolling mean along the wavelength axis (over 10 adjacent points). The result of this postprocessing steps is shown by the purple circles in Fig. 7. Hereafter low pass filtering of the relative transmission with $f_C = f_s/10$ was applied for a slight smoothing (green stars). This reduces high frequency signal fluctuations which are for example caused by reflections and optical cavities along the optical path. For example, the two grating couplers cause internal reflections due to the refractive index modulation needed for the functionality of the gratings.

3.2 Wavelength calibration using a $H^{13}C^{14}N$ reference gas cell

Following the data pre-processing described in the previous section (Sec. 3.1), the transmission of the hydrogen cyanide ($H^{13}C^{14}N$) gas cell at 3.3 kPa (25 Torr) was used to perform the wavelengths calibration. Due to the rotational-vibration absorption of $H^{13}C^{14}N$, the spectrum of the gas cell shows 54 absorption lines, which could solve as a low-uncertainty wavelength reference [17]. Therefore, it is necessary to determine the centres of the absorption

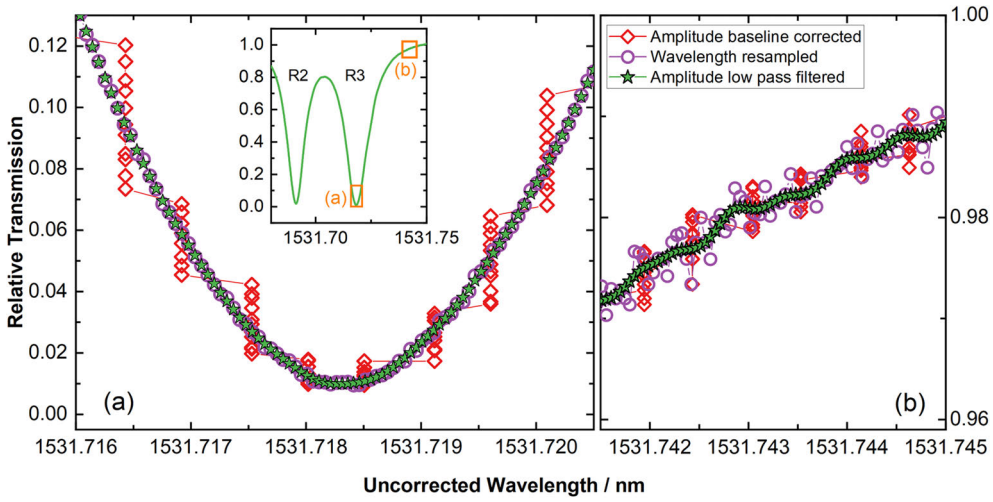

Figure 7: Data processing of the baseline corrected data (wavelengths and amplitudes) for two section of the PIC spectrum. (a) Peak of the ring 3 resonance and (b) off-resonance. The diamonds show the raw data signal after baseline correction. The circles show the signal amplitude after resampling of the wavelength scale from 10 values every 0.5 pm to a continuously wavelength scale with uniform wavelength steps of 0.05 pm. To reduce high frequency noise, the data is slightly smoothed with a low pass filter as shown with stars.

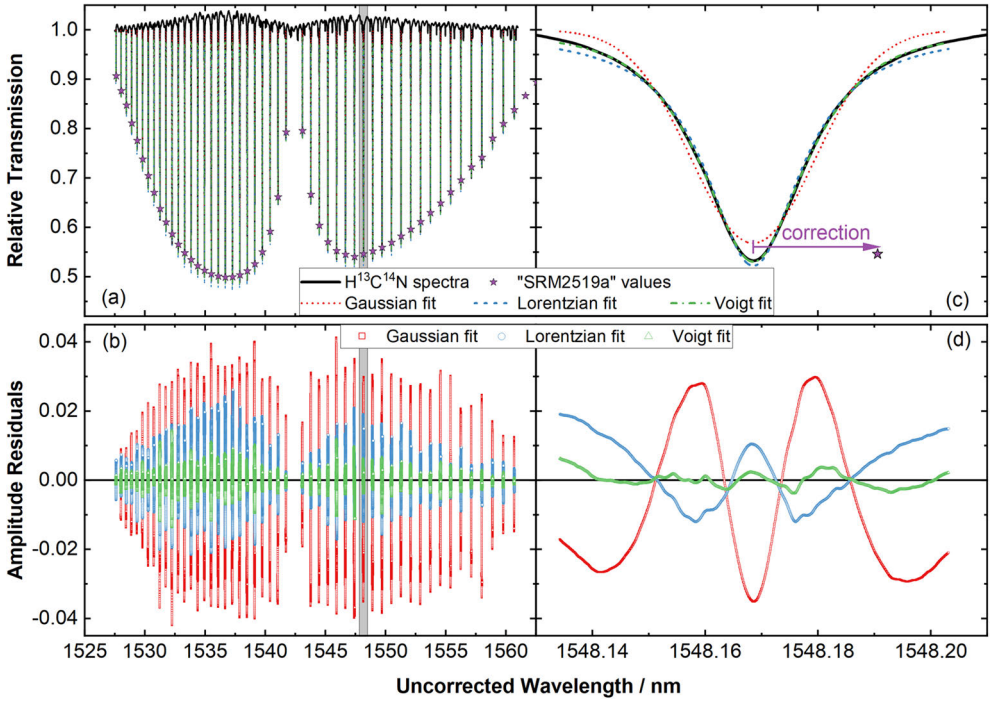

Figure 8: (a) Relative transmission (black) of the hydrogen cyanide $H^{13}C^{14}N$ gas cell together with the positions of the line centres according to SRM 2519a (stars) [17]. Determine Gaussian (red), Lorentzian (blue) and Voigt (green) fit for each line in the spectral region from 1527.5 nm to 1562 nm. (b) Comparison of the amplitude residuals for each fit function. (c–d) Section of the spectrum (a) fit residuals (b) around the P8 line.

lines as shown in Fig. 8. According to the SRM 2519A a Lorentzian or Voigt line shape least square fitting is suitable for high-accuracy calibration with uncertainty below 3 pm [17]. Compared to the Lorentz function, the Voigt fitting is more complex because of the convolution of a Gaussian and a Lorentzian part. To estimate the influence of the fit model to the determined line centre we compared a Gaussian, Lorentzian and Voigt fit. In the first step, a simple and fast peak detection (local minimum) is used for the first estimation of the centres and the full width

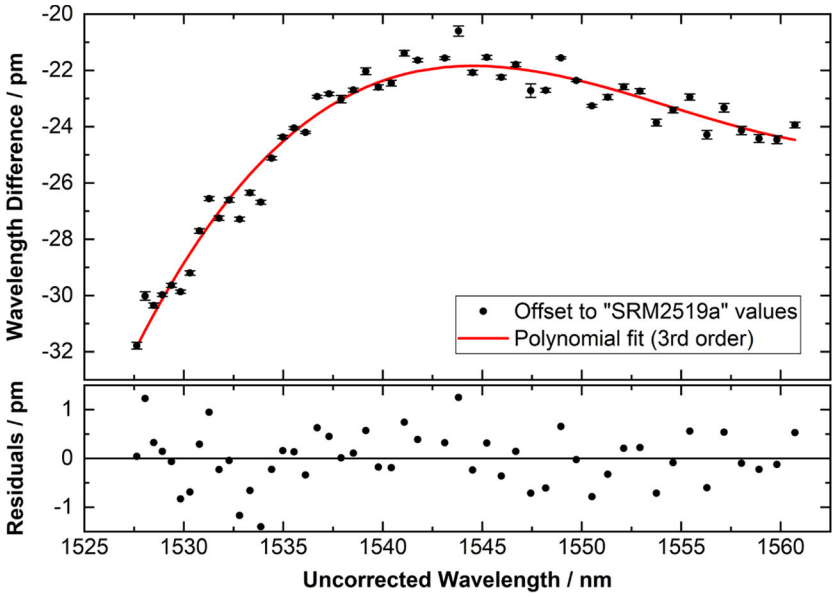

Figure 9: (upper) Difference between the centre wavelength of absorption lines determine by the Voigt fit and the literature values with uncertainty (whisker) from [17]. Polynomial fit (3rd order) used for the wavelength correction of the spectrum (red line). (lower) Residuals of the fit function.

half maximum (*FWHM*). Using this initial information, a least square fit optimisation is performed for each of the lines using all three fit models. The resulting fits for each of the lines are shown in Fig. 8a for the full spectrum and in Fig. 8c for the P8 line.

Figure 8b shows the amplitude residuals between each fit and the determined gas cell spectra. The Voigt function shows the best match with the absorption line spectra and therefore has the lowest amplitude residuals. Comparing the differences between Voigt fit model-based line centre detection we determined a max difference of 0.52 nm for a simple local minima peak detection, 0.32 pm for Gauss fit and 0.20 pm for Lorentz fit. The deviation of 0.2 pm between Voigt and Lorentz fit therefore provides a reasonable estimation of our peak fit uncertainty. We further determined the computing time required for each method. The detection of local minima is clearly the fastest method with approx. 50 ms, followed by the Gauss and Lorentz fit with approx. 100 ms. Due to the higher complexity of the Voigt model, the data processing took about 300 ms. For real-time applications using fast wavelength scan rates, this three times higher processing time could be a limiting factor and the Lorentz fit is a suitable alternative.

After the line centre determination, the wavelength differences between the detected centre (by Voigt fit) and the SRM 2519a literature values [17] are calculated as illustrated in Fig. 8c. Figure 9 shows an example of these differences as a function of the uncorrected wavelength. For the wavelength correction a 3rd order polynomial fit, weighted with the uncertainty of each absorption line (SRM 2519a values [17]), was performed (red line).

The lower graph shows the resulting residuals, with a typical standard deviation of approx. 0.6 pm (using a dataset of 20 measurements). Hence, we can correct the wavelength scale in the shown example with $\Delta\lambda = (22.0 \ldots 31.4)\,\text{pm} \pm 0.6\,\text{pm}$. Considering the accuracy of the wavelength reference data of <0.1 pm [17] together with our typical fit residuals we estimate a combined wavelength uncertainty of typically 0.6 pm.

It should be mentioned that the wavelength calibration is also possible without prior information about the approximate wavelength. As described in [6] it is possible to perform an absorption line detection and use the wavelength gap between the R0 and P1 absorption line of 1.3614 nm as a marker to calibrate the wavelength. Comparing this approach with our method, some advantages and disadvantages can be identified.

One advantage of the method of [6] is that the measurement effort is lower, since no “uncalibrated” wavelength has to be determined and processed. The achievable measurement uncertainty should be comparable for both methods. An advantage of our method is that the wavelength calibration is also possible without the marker (R0 to P0). For example, if only the R or the P branch or only some peaks of the gas cell spectrum are measured. In addition, the integrity of the continuous tuning of the

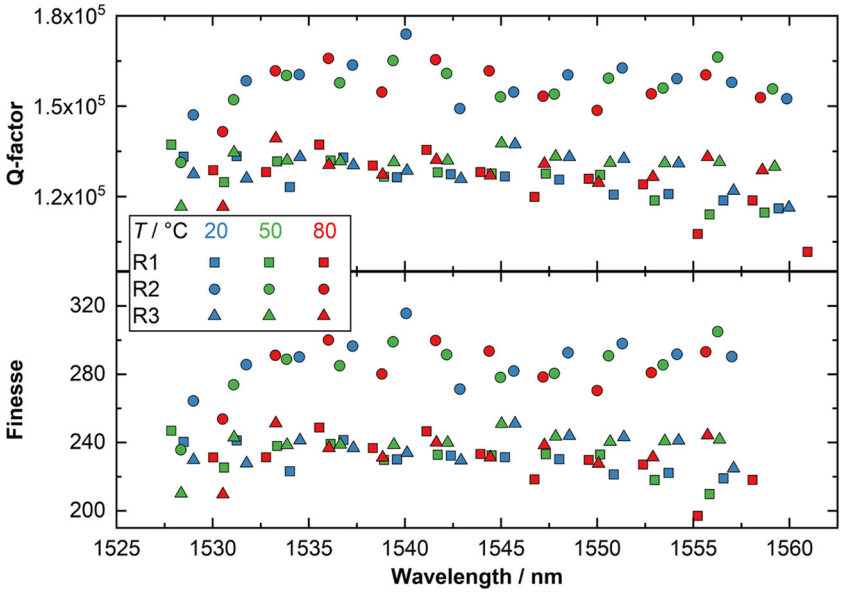

Figure 10: Q-factor (upper) and finesse (lower) of the three ring resonators for different surface temperatures of the temperature-controlled platform.

laser wavelength is difficult to verify when only the amplitude values are recorded. Errors during the measurement process for example due to mode jumps, can remain undetected.

4 Results and discussion

4.1 Temperature-dependent ring resonator spectrum

In the following, we have investigated the temperature-dependent shift of the resonance wavelength of the three ring resonators connected to a single bus waveguide (see insert in Fig. 11). Therefore, we determined the spectrum for 3 different temperatures 20 °C, 50 °C and 80 °C. All data were processes as previously described (Sec. 3) including the wavelength calibration (comparable to Fig. 9).

A typical approach to determine the position of the ring resonator peak is by using a Lorentzian function (comparable to Fig. 8 for the gas cell) to fit the resonance [13]. Using this Lorentzian fit for each resonance within the spectrum (see Fig. 7) we determined the central wavelength λ_m and the *FWHM* of the resonances. Since the peak shape of the ring resonators is not determined by first principles, like the gas absorption spectra, there exists no pre-defined fit model. To estimate an upper bound for the uncertainty of the ring resonator peak fits, we use a similar approach as for the gas cell (see Fig. 8) by comparing the peak centre results of 4 different models (fit with Gaussian, Lorentzian and Voigt function, and minimum of pre-processed date). With this approach, we also consider effects arising from non-perfect baseline corrections and fluctuations of the coupling (see Fig. 5), as the models react differently here. The resulting standard deviations of peak position values were analysed for over 160 individual peak detections. A upper limit (mean + 2σ) of the peak differences of 0.3 pm was determined and leads to an uncertainty contribution of 4.1 mK (see Tab. 2).

Using the determined central wavelength λ_m and the *FWHM* of the resonances we calculate the quality factor Q and the finesse $\mathcal{F}$ for each peak (see Eqs. (1), (2)), which are measures of the sharpness of the peaks and their relative spacing. As Fig. 10 clearly shows, resonator R2 has both the highest quality factor and finesse (see Tab. 1). Since R2 has the largest round trip length and biggest gap, we assume that the coupling of R1 and R3 is slightly to high (over cou-

Table 1: Design parameter of the notch filter type ring resonators used for the experiments. Experimentally determined mean Q-factor and finesse with their standard deviation over the investigated wavelength range for all three temperatures.

	R1	R2	R3
Radius / µm	35.037	35.149	35.048
Gap / nm	470	500	485
Mean Q-factor / 1000	125 ± 8	157 ± 8	130 ± 6
Mean Finesse $\mathcal{F}$	229 ± 11	285 ± 15	237 ± 10

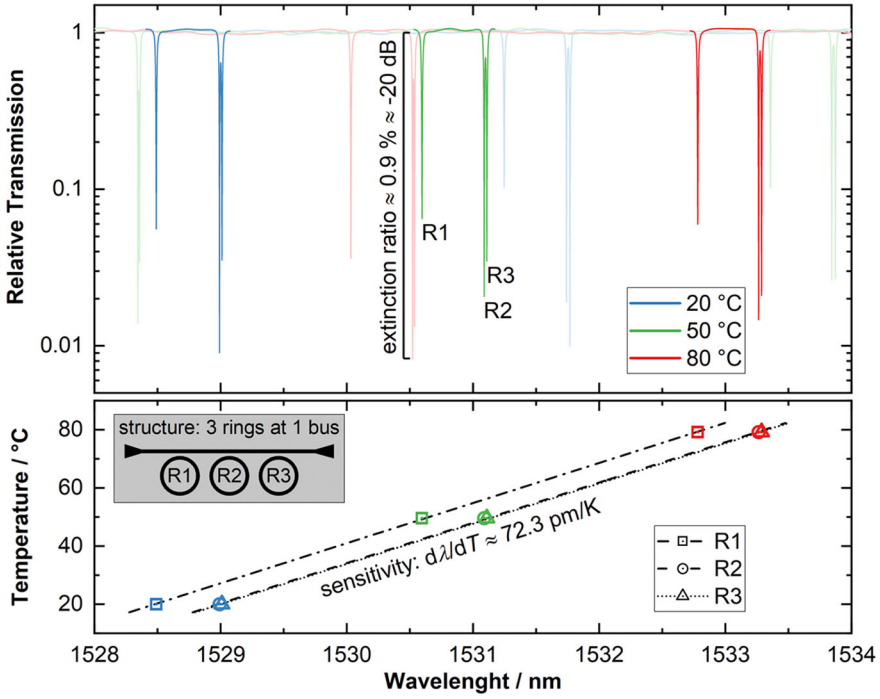

Figure 11: (upper) Relative transmission of the PIC for three exemplary temperatures of the thermostat platform. (lower) Temperature-dependent shift of the resonance wavelength for each of the three ring resonators.

pling). Therefore, R2 should be close to critical coupling, where the coupling power and roundtrip loss are equal. Within this temperature range there is no significant effect of temperature on the Q-factor and the finesse.

Figure 11 (upper part) shows a 6 nm wide section of the transmission spectrum for the temperatures 20 °C, 50 °C and 80 °C of the thermostat platform. These temperatures are determined as described in Sec. 2.3 with the Pt100 reference sensor. For a better overview one resonance order was highlighted in the graph. As a result of the three temperature steps of about 30 K a resonance wavelength shift of approx. 2.2 nm could be observed. It should be note that the temperature difference between the Pt100 and the PIC was not considered.

A comparison of the extinction ratios of the individual resonances shows an attenuation of the transmission by up to a factor of 100 or 20 dB. The difference in extinction ratio of the three resonators mainly results from the coupling gap of each resonator to the shared bus waveguide (see Tab. 1). The peak positions in relation to the temperature are shown in the lower part of Fig. 11. Each line represents the linear fit for the wavelength change over temperature. The determined linear slope or temperature sensitivity is approx. 72.3 pm/K. This result is comparable to the experimental findings of other groups [2, 13, 14, 20].

4.2 Discussion of uncertainty components and noise sources

Figure 12 show the spectral density of different noise sources (temperature and transmission) using comparable datasets as shown in the previous sections (shown in Fig. 4 and Fig. 5). All temperature dependent datasets were recorded at 20 °C and the wavelength values were transformed to temperature using the determined factor of 72.3 pm/K.

For long time intervals of several minutes and more, the fluctuation of the thermostat temperature is the dominant temperature noise source with of approx. 10 mK/$\sqrt{\text{Hz}}$. Within the timescale of a single measurement between 0.1 s to 10 s (grey marked in Fig. 12) the dominant uncertainty is caused by the wavelength calibration of the spectrum (scan) with 8.2 mK or 0.6 pm (see Sec. 3.2). The main reason for this uncertainty is related to the inhomogeneous change of the wavelength during the scanning of a spectrum. To avoid this measurement uncertainty, it is possible to lock the wavelength to a frequency comb as described in [21].

Another in Sec. 2.1 mentioned possibility is to lock the laser wavelength to a single resonance in a constant power mode as shown in [18]. For a first evaluation of this method using our setup, we determined the spectral noise for a constant wavelength using a wavemeter (purple

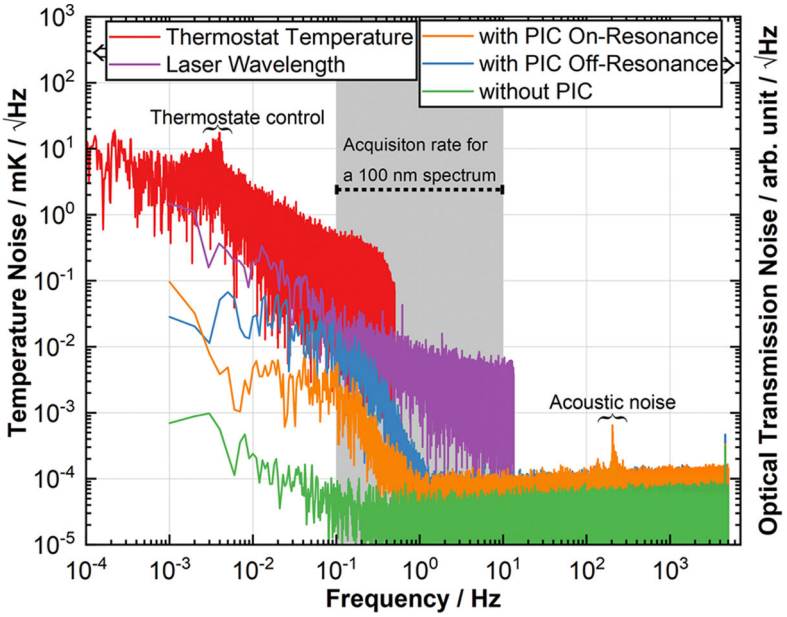

Figure 12: Amplitude spectral density of the surface temperature of the thermostat platform (red) together with the laser wavelength changes converted to mK (using the coefficient 72.3 pm/K). Optical amplitude noise of the laser power without PIC (green) and with PIC for a measurement at the resonator resonance wavelength (on-resonance) and out-of-resonance (off-resonance).

graph in Fig. 12). Using the factor of 72.3 pm/K, the corresponding temperature noise would be between 50 µK/$\sqrt{\text{Hz}}$ and 6 µK/$\sqrt{\text{Hz}}$ at a sampling rate in the range of 0.1 Hz to 10 Hz. Another relevant factor for constant power operation (resonance locking) is the coupling stability and the associated fluctuation in the transmission. Comparable to Sec. 2.4 we determined the transmitted laser power with PIC (on- / off-resonance) and without PIC (see Fig. 12). The green curve shows the transmission without PIC, which obviously provides the lowest transmission noise. Due to the thermal fluctuations, the coupling between the fibres and the PIC changes. Consequently, the transmission noise including the PIC is higher and increase with increasing temperature noise even for the PIC off-resonance (orange in Fig. 12). Since the photonic resonator itself is temperature-sensitive, the transmission noise is higher compared to off-resonance measurement for sampling rates up to approx. 1 Hz. The transmission noise for the on- / off-resonance are comparable for higher sampling rates (>1 Hz). This is because the temperature fluctuations decrease, and other noise sources become more important (e. g. acoustic noise). An example of this noise is the peak around 200 Hz, which is mainly caused by our vacuum tweezers.

All previously discussed uncertainty contributions within a typical measurement interval are summarised in Tab. 2. Considering the uncertainty contributions marked in bold, our setup shows a repeatability of 10 mK in the range from 10 °C to 90 °C.

For the later sensor application and the finale ITS-90 tracible calibration of the PIC-based thermometer further uncertainty contributions have to be take into account, like effects arriving from packing (ageing or drift) [9], the potentially different thermal contact of the Pt100 and the photonic chip, or the residuals of a fitted temperature-wavelength function. These contributions will be investigated and discussed in our future work, while in this paper we have focused on the precise characterisation of the measurement setup.

5 Summary and outlook

In this paper, we proposed a measuring set-up suitable for the thermal and optical characterisation of photonic thermometers in the temperature range from 10 °C to 90 °C. Using two thermostats in series a long-term thermal stability of the temperature-controlled platform of approx. 2.6 mK was determined at 30 °C for a duration of 24 h. Statistical analysis of the temperature fluctuation within a typical acquisition time (10 s) for a 100 nm spectrum show a stability of the surface temperature better than 0.51 mK for 20 °C and 4.2 mK for 90 °C. Using a $H^{13}C^{14}N$ gas cell an in-situ calibration of each PIC spectrum was performed with a

Table 2: Summary of the discussed uncertainty contribution within a typical measurement interval of 10 s for the swept wavelength based photonic thermometry sensing method.

Source	Value	Uncertainty Contribution ($k = 1$) / mK
Temperature-Controlled Platform (mean + 2σ of short-term standard deviations, see Fig. 4)	0.46 mK @ 20 °C	0.46 @ 20 °C
	4.2 mK @ 90 °C	**4.2** @ 90 °C
ITS-90 calibration of Pt100	8.2 mK	8.2
Wavelength stability (see Fig. 12)	<3.6 fm	<**0.05**
Wavelength calibration (typical standard deviation, see Fig. 9)	600 fm	**8.2**
Resonator peak fit, including coupling stability from Fig. 5 (mean + 2σ of peak difference standard deviations, see Sec. 4.1)	300 fm	**4.1**
Packaging (ageing or drift), T_{chip} vs. T_{Pt100}, $T(\lambda)$-fit (see text)	Unknown	Unknown
Repeatability (includes bold printed values)		≤**10**

typical uncertainty of 0.6 pm. Results show a high optical quality of the ring resonators with an average of 157 000 together with high extinction ratios of up to 20 dB between 1525 nm and 1565 nm. A temperature sensitivity of the ring resonators of approx. 72 pm/K could be determined.

An analysis of the different uncertainty contributions shows a repeatability of our measuring set-up better than 10 mK in temperature range from 10 °C to 90 °C. For a complete determination of the uncertainty budget some aspects need further investigation, like packaging and ageing. Nevertheless, our results and findings provide a good starting point and are promising for the goal of a photonic ring resonator-based temperature sensor.

Funding: This work was carried out within the framework of the project PhotOQuant (17FUN05), which has received funding from the EMPIR programme co-financed by the Participating States and from the European Union's Horizon 2020 research and innovation programme.

References

1. DIN EN 60751:2009-05, Industrial platinum resistance thermometers and platinum temperature sensors, doi: 10.31030/1507857.
2. Z. Ahmed, et al.: "Photonic thermometry: upending 100 year-old paradigm in temperature metrology", In: Proc. SPIE 10923, Silicon Photonics XIV, 109230L, 2019, doi: 10.1117/12.2505898.
3. G.-D. Kim, et al.: "Silicon photonic temperature sensor employing a ring resonator manufactured using a standard CMOS process", Opt. Express 18, 22215–22221 (2010), doi: 10.1364/OE.18.022215.
4. S. Dedyulin, et al.: "Packaging and precision testing of fiber-Bragg-grating and silicon ring-resonator thermometers: current status and challenges". Meas. Sci. Technol. 31, 074002 (2020), doi: 10.1088/1361-6501/ab7611.
5. J. L. de Miguel, et al.: "Experimental demonstration of low-uncertainty calibration methods for Bragg grating interrogators". Sensors 18(6), 1895 (2018) doi: 10.3390/s18061895.
6. X. Fan, et al.: "Self-marked HCN gas based FBG demodulation in thermal cycling process for aerospace environment", Opt. Express 26, 22944–22953 (2018), doi: 10.1364/OE.26.022944.
7. K. Hicke, et al.: "Enhanced distributed fiber optic vibration sensing and simultaneous temperature gradient sensing using traditional C-OTDR and structured fiber with scattering dots". Sensors 19(19), 4114, 2019, doi: 10.3390/s19194114.
8. C. Zhang, et al.: "Photonic thermometer with a sub-millikelvin resolution and broad temperature range by waveguide-microring Fano resonance". Opt. Express 28, 12599–12608 (2020), doi: 10.1364/OE.390966.
9. N. Klimov, et al.: "Towards replacing resistance thermometry with photonic thermometry". Sensors and Actuators A: Physical 269, 308–312 (2018), doi: 10.1016/j.sna.2017.11.055.
10. J. Tao, et al.: "An ultrahigh-accuracy miniature dew point sensor based on an integrated photonics platform". Sci. Rep. 6, 29672 (2016), doi: 10.1038/srep29672.
11. www.vtt.fi/sites/photoquant/, last accessed: 05.03.2020.
12. L. Zimmermann, et al.: "BiCMOS silicon photonics platform". in Optical Fiber Communication Conference, OSA Th4E.5., 2015, doi: 10.1364/OFC.2015.Th4E.5.
13. W. Bogaerts, et al.: "Silicon microring resonators", Laser & Photonics Reviews 6(1), 47–73 (2012), doi: 10.1002/lpor.201100017.
14. D. G. Rabus, et al.: "Ring Resonators: Theory and Modeling". Springer Series in Optical Sciences, Vol. 127. Springer, Cham (2020), doi: 10.1007/978-3-030-60131-7_2.
15. L. M. Weituschat, et al.: "Photonic and thermal modelling of microrings in silicon, diamond and GaN for temperature sensing". Nanomaterials 10(5), 934 (2020), doi: 10.3390/nano10050934.
16. W. Dickmann, et al.: "Heat dynamics in optical ring resonators", In: Proc. SPIE 11783, Optical Metrology VIII, 1178309 (2021), doi: 10.1117/12.2592552.
17. S. L. Gilbert, et al.: "Hydrogen Cyanide H13C14N Absorption Reference for 1530 nm to 1565 nm Wavelength Calibration – SRM 2519a", NIST Special Publication 260-137, 2005 ed, in press.

18. H. Xu, et al.: “Ultra-sensitive chip-based photonic temperature sensor using ring resonator structures”. Opt. Express 22, 3098–3104 (2014), doi: 10.1364/OE.22.003098.
19. DKD Richtlinie DKD-R 5-1: “Kalibrierung von Widerstandsthermometern”, Ausgabe 09/2018, doi: 10.7795/550.20180828AC.
20. D. Taillaert, et al.: “Grating couplers for coupling between optical fibers and nanophotonic waveguides”, Jpn. J. Appl. Phys. 45, 6071 (2006), doi: 10.1143/JJAP.45.6071.
21. R. Gotti, et al.: “Comb-locked frequency-swept synthesizer for high precision broadband spectroscopy”. Sci. Rep. 10, 2523 (2020), 10.1038/s41598-020-59398-1.

Bionotes

René Eisermann
Physikalisch-Technische Bundesanstalt (PTB), Abbestr. 2–12, 10587 Berlin, Germany
rene.eisermann@ptb.de

René Eisermann is a research scientist at the Physikalisch-Technische Bundesanstalt. He graduated in engineering at the University of Applied Sciences Brandenburg and in physics at the Brandenburg University of Technology Cottbus. Since 2010 he works in the field of photonic integrated circuits and fibre optical sensing. He joined PTB in 2019 where he currently works on his Ph.D. His research focus on the application of fibre optical sensing for localized and distributed sensing and integrated photonic sensors.

Stephan Krenek
Physikalisch-Technische Bundesanstalt (PTB), Abbestr. 2–12, 10587 Berlin, Germany
stephan.krenek@ptb.de

Stephan Krenek is leader of the working group Photonic Thermometry at the Physikalisch-Technische Bundesanstalt. He graduated in physics at the TU Dresden. Since 2008, he is researcher at PTB, where he did his PhD in the field of radiation thermometry and the measurement of thermo-physical material properties. Since 2014, he is working in the Temperature department, where his current research focus is on the application of photonics for temperature measurement, e.g. with fibre optical sensing and integrated photonic sensors.

Georg Winzer
Leibniz-Institut für innovative Mikroelektronik (IHP), Im Technologiepark 25, 15236 Frankfurt (Oder), Germany
winzer@ihp-microelectronics.com

Georg Winzer received his Diploma in electrical engineering from Technische Universität Berlin, Germany in 2012. Since 2012 he works for the IHP - Leibniz-Institut für innovative Mikroelektronik, Frankfurt (Oder), Germany. His research interests include the design and layout of PIC and EPIC devices and their characterization and the setup of a photonic design kit.

Steffen Rudtsch
Physikalisch-Technische Bundesanstalt (PTB), Abbestr. 2–12, 10587 Berlin, Germany
Steffen.Rudtsch@ptb.de

Steffen Rudtsch is head of the temperature department at the Physikalisch-Technische Bundesanstalt. He graduated in physics at the University of Leipzig and completed his doctorate in thermophysics at the Brandenburg University of Technology Cottbus. His research focuses on temperature fixed points, sensors and methods for contact thermometry and the measurement of thermophysical material parameters.